

GenHel S-76C Model Correlation using Flight Test Identified Models

Chris Quiding
 Handling Qualities Engineer
 Sikorsky Aircraft Corporation
 Stratford, C
 cquiding@sikorsky.com

Christina M Ivler
 Aerospace Engineer
 Aeroflightdynamics Directorate (AMRDEC)
 US Army Research, Development, and Engineering
 Command
 Ames Research Center, Moffett Field, CA
 civler@mail.arc.nasa.gov

Dr. Mark B. Tischler
 Senior Scientist and Flight Control Group Lead
 Aeroflightdynamics Directorate
 US Army Research, Development, and Engineering
 Command
 Ames Research Center, Moffett Field, CA
 mtischler@mail.arc.nasa.gov

Abstract

A flight test program using a Sikorsky S-76C++™ test aircraft was conducted in October 2006 at the Sikorsky Flight Test Development Center in West Palm Beach, FL. This flight testing was performed in support of the S-76D™ program. The S-76D incorporates a new automatic flight control system (AFCS). In order to support design of the AFCS, one of the major goals for this flight test program was to collect data for model identification. The identified models were then to be used both directly for S-76D AFCS design and as tools for assisting with correlation of the GenHel S-76C model. The changes made to the GenHel S-76C model were then used to update the GenHel S-76D model. In this paper two of the S-76C++ identified models are examined along with the updates made to the GenHel S-76C model.

Nomenclature

a_x, a_y, a_z	X, Y and Z direction accelerometers (body-axis coordinate system)	u_m, v_m, w_m	X, Y and Z direction velocities @ accelerometer location (body-axis coordinate system centered @ accelerometers)
a_{x_m}, a_{y_m}	X and Y direction accelerometers @ accelerometer location (body-axis coordinate system centered @ accelerometers)	u_o, v_o, w_o	Trim X, Y and Z direction velocities (body-axis coordinate system)
$(a_{y_m})_2$	Equivalent to a_{y_m} , but used over a separate frequency range	x_e	Engine state
e	Main rotor hinge offset	K_p, K_q	Scaling factors for lead-lag filters
g	Gravitational acceleration	R	Main rotor radius
p, q, r	Roll, pitch and yaw rates (body-axis coordinate system)	X_A, X_B, X_C	Lateral, longitudinal and collective stick positions
u, v, w	X, Y and Z direction velocities (body-axis coordinate system)	X_p	Pedal position
		Z_{cg}	Vertical distance between aircraft center of gravity location and accelerometer location
		α	Freestream aircraft angle of attack
		β	Freestream aircraft sideslip
		$\beta_o, \beta_{1s}, \beta_{1c}$	1/rev rotor flapping coefficients (multi-blade coordinate system)

*Presented at the American Helicopter Society 64th Annual Forum, Montréal, Canada, April 29 - May 1, 2008.
 Copyright © 2008 by the American Helicopter Society International, Inc. All rights reserved.*

γ	Lock number
ζ_{llr}	Lag regressive mode damping ratio
ζ_p, ζ_q	Damping ratios of lead-lag dipole numerators
η_{CT}	Integrated perturbation thrust coefficient
$\eta_{XC'}$	Lagged collective state
θ, ϕ, ψ	Pitch, roll and yaw attitudes (earth-fixed coordinate system)
ν	Rotor inflow
ν_ζ	Lag regressive mode frequency in rotating frame
σ_{llr}	Real part of lag regressive mode eigenvalue
τ_f	Flapping time constant
$\omega_{d_{llr}}$	Imaginary part of lag regressive mode eigenvalue
ω_{llr}	Lag regressive mode natural frequency
ω_p, ω_q	Natural frequencies of lead-lag dipole numerators
Ω	Main rotor speed

Introduction

The Sikorsky S-76[®] is a light twin-engine helicopter originally designed and certified in the 1970s. Subsequent updates have been undertaken on the S-76 over the last 30 years to increase the capability of the aircraft. The S-76B[™] was designed and certified in the early 1980s and the S-76C[™] was designed and certified in the early 1990s. While the S-76 has been successful in military, search & rescue and EMS applications, its primary missions are offshore oil transport and executive/VIP transport.

The S-76D shown in Fig. 1 is the latest update of the S-76. Among the several new features of the S-76D are a Sikorsky 4th generation main rotor, quiet tail rotor, Pratt and Whitney Canada PW210S[™] engines, a Thales glass cockpit and a Thales automatic flight control system (AFCS).

The 4-axis AFCS designed by Thales will provide basic functions as well as a flight director mode. The design of a flight control system that provides good flying qualities and is robust to uncertainties requires a good math model for the aircraft. Also, considering that the AFCS supplier had no previous experience with S-76, it was especially important to provide accurate, high fidelity models.

A frequency response flight test program using a fully instrumented S-76C++ test aircraft was conducted in October 2006 at the Sikorsky Flight Test Development Center in West Palm Beach, FL. One of the major goals of this flight test program was to collect data for model identification. The identified models were then to be used as design tools for the S-76D AFCS as well as to help correlate the GenHel S-76C model. The changes made to correlate the GenHel S-76C model were then incorporated into the GenHel S-76D model to further support design and development of the S-76D AFCS.

This paper will address both the model identification and the updates made to the GenHel S-76C model. The model identifications covered will be those performed at hover and 120 knots level flight. For both model identifications, frequency domain system identification methods using the CIPHER[®] software (Ref. 1) were used.

The updates to the GenHel S-76C model covered in this paper will be the determination of the aerodynamic phase lag for correction of pitch-roll coupling prediction and the inclusion of a destabilizing yaw damping map to bring Dutch Roll damping closer to that observed in flight.

Overview of Model Identification Methods

As discussed in the introduction of this paper, frequency domain system identification methods using the CIPHER[®] software (Ref. 1) were chosen for the S-76C++ model identifications. Frequency domain methods are particularly well suited to the helicopter problem as discussed in Ref. 1 because dynamically unstable aircraft (such as helicopters) can be identified, uncorrelated noise in the system drops out of the frequency response calculation, accuracy is easily interpreted via the coherence function and the model can be fit only over accurate frequency ranges. These methods have been successfully used to identify dynamics for many helicopters including the UH-60 (Ref. 2), Bo-105 (Ref. 3), AH-64 (Ref. 4), and the Bell Armed Reconnaissance Helicopter (Ref. 5).

The basics of the system identification process using CIPHER[®] can be described by the following three steps:

1. Frequency Response Identification from Flight data
CIPHER[®] employs an overlapping windowed chirp-Z transform, an efficient and flexible FFT, to perform the conversion of the time history data to the frequency domain. Multi-input analysis is then performed to condition out the effects of off-axis input from the pilot during the frequency sweeps. Finally, the final frequency response is determined by using a composite window function that combines the frequency responses from 5 windows into a single response with coherence weighting. The calculations are described in detail in Ref 1.

2. State Space Model Identification

Model parameters are optimized to provide the best match to frequency responses identified from flight data. A coherence weighted cost function (J) is used to quantify the match between flight data and the state-space model. Then the theoretical accuracy parameters, Insensitivity (I) and Cramer Rao Bound (CR), are used to evaluate the uniqueness of each parameter. Insensitivity is measure of the insensitivity of the cost function to a percent change in the identified parameter. A Cramer Rao Bound is the estimated minimum standard deviation of a parameter that would be calculated after many repeated trials.

3. Time Domain Verification

The state-space model is driven with flight data (not used in the identification), and the outputs of the model are evaluated against the real flight data. Doublets in each axis are usually used for verification.

This paper will discuss these steps for both the hover and 120 kts identifications of the S-76C++ helicopter.

Hover Model Identification

The hover model was identified using piloted frequency sweeps of the longitudinal cyclic stick, lateral cyclic stick, collective stick and pedals respectively. Frequency sweep techniques developed over many years of system identification work by the U.S. Army Aeroflightdynamics Directorate (AFDD) were employed in these flight tests. These methods are described in Ref. 1. The S-76C++ test aircraft was fully instrumented during the flight tests and the hover model identification flight test data was sent to AFDD for a hover higher order hybrid model identification. Sikorsky did parallel quasi-steady model identification at hover (6 DOF) for comparison purposes, but the results are not shown herein.

Frequency Response Determination

Frequency responses were identified from flight data using the methods discussed in the previous section of this paper. For the analysis, the input signals were the piloted inputs X_A , X_B , X_C and X_p . The output signals were p , q , r , a_x , a_y , a_z , \dot{u} , \dot{v} and \dot{w} . The velocity derivative signals \dot{u} , \dot{v} and \dot{w} were reconstructed using the kinematic relationships shown in the following equations.

$$\dot{u} = a_x - g\theta - qw_0 + rv_0 \quad (1)$$

$$\dot{v} = a_y + g\phi - ru_0 + pw_0 \quad (2)$$

$$\dot{w} = a_z - pv_0 + qu_0 \quad (3)$$

Note that at hover, $\dot{w} \cong a_z$.

The identified frequency responses are not pictured here for brevity. As an example of the results of the frequency-response identification, see Figs. 6 – 8 later in the report (the solid lines are the identified frequency responses referred to here). The high quality of these frequency responses is indicated by their smooth shape and good coherence.

Model Structure Determination

Determining the appropriate model order is an important step to take before beginning system identification. The importance of including higher-order dynamics in the model structure can often be determined by inspection of the frequency responses over the frequency range of interest. The following sections of the paper describe the importance of the inclusion of higher-order dynamics including coupled flap/fuselage dynamics, lead-lag dynamics, engine dynamics, and inflow-coning dynamics in the S-76 hover model structure.

Flap/Fuselage Dynamics

For helicopters with moderate flap stiffness such as the S-76, the on-axis responses (q/X_B and p/X_A) are well modeled by a 6DOF approximation for frequencies up to 8-10 rad/s. However, a 6DOF model usually does not accurately capture the phase characteristic for the off-axis responses p/X_B and q/X_A . A model structure that explicitly models the rotor flapping dynamics better predicts these off-axis responses, as well as extends the frequency range of applicability. To illustrate this point, example results are shown for model fitting with a 6DOF model and with a hybrid model that includes flapping dynamics for the S-76. Figure 2 shows a comparison of p/X_B for the quasi-steady model vs. the higher order model with flapping dynamics. This figure indicates that the off-axis response p/X_B is much better represented by the model that includes flapping dynamics, as seen by the much improved match to flight data magnitude and phase. The same characteristic can be seen for the AH-64 dynamics in Ref. 1.

Since off-axis responses are important for the AFCS design and the GenHel S-76C model correlation, the coupled flapping/fuselage dynamics were included in the model structure.

Lead-Lag Dynamics

The effect of the lead-lag dynamics can be clearly seen in the piloted frequency response of Fig. 3 between 20-30 rad/sec. The regressive lag mode (or lead-lag dynamics) looks like a notch in the magnitude response, accompanied by a large phase shift at roughly 24 rad/s.

The lag regressive mode was important for the S-76 AFCS design, therefore a representation of the lead-lag dynamics was included in the model structure.

Engine Dynamics

As shown in Fig. 4, the r/X_C phase rolls off very quickly at high frequencies. This is well known (see Ref .1) as an effect associated with engine dynamics. These dynamics can be modeled as a time delay on the r/X_C pairing. Thus, a padé approximation was included in the state-space model structure to represent the engine effect on the yaw response.

Coning-Inflow Dynamics

Figure 5 shows the response of vertical acceleration (a_z) to collective input for the hover flight condition. The rising magnitude response above about 2 rad/s is the result of the coning-inflow dynamics. This rise in magnitude cannot be represented within a quasi-steady model structure. Therefore, a representation of coning-inflow dynamics were necessary in the model structure.

Hybrid Model Structure

The hybrid model structure discussed in Ref. 1 was used for this model identification. The term “hybrid” indicates that the low frequency velocity effects are represented by quasi-steady derivatives (e.g. L_v and M_u), while short term dynamics are modeled with explicit rotor states and associated derivatives (e.g. $L_{\beta_{1s}}$).

The hybrid S-76 model was identified with flapping dynamics, coning-inflow dynamics, and engine dynamics. The lag-regressive mode dynamics were identified in the model as a filter on the rate outputs. The equations for the model are given in Ref 1.

The model structure used for identification is:

$$M\dot{x} = Fx + Gu \quad (4)$$

$$y = H_0x + H_1\dot{x} \quad (5)$$

The state, input and output vectors for this model identification are:

$$x = [u \ v \ w \ p \ q \ r \ \phi \ \theta \ \beta_{1s} \ \beta_{1c} \ u_m \ v_m \ v \ \dot{\beta}_0 \ \beta_0 \ \eta_{CT} \ x_e \ \eta_{X_C}] \quad (6)$$

$$u = [X_A \ X_B \ X_C \ X_P] \quad (7)$$

$$y = [\dot{u}_m \ \dot{v}_m \ \dot{w} \ p \ q \ r \ a_{x_m} \ a_{y_m} \ a_z \ (a_{y_m})_2] \quad (8)$$

The measured accelerations were not taken at the vertical center of gravity, therefore an estimate of the vertical c.g. offset of the measurement (Z_{accel}) was identified in the state equations:

$$\dot{u}_m - \dot{u} - \dot{q}Z_{accel} = 0 \quad (9)$$

$$\dot{v}_m - \dot{v} + \dot{p}Z_{accel} = 0 \quad (10)$$

The lead-lag dynamics primarily influence the on-axis responses in pitch rate and roll rate and can be well represented as a complex dipole. This dipole is applied as a filter on the on-axis angular responses to the lateral and longitudinal stick inputs. The transfer functions used to perform this fit are presented below.

$$\left(\frac{q}{X_B}\right)_{lead-lag} = \left(\frac{q}{X_B}\right) * \left(\frac{K_q(s^2 + 2\zeta_q\omega_q s + \omega_q^2)}{s^2 + 2\zeta_{lr}\omega_{lr} s + \omega_{lr}^2}\right) \quad (11)$$

$$\left(\frac{p}{X_A}\right)_{lead-lag} = \left(\frac{p}{X_A}\right) * \left(\frac{K_p(s^2 + 2\zeta_p\omega_p s + \omega_p^2)}{s^2 + 2\zeta_{lr}\omega_{lr} s + \omega_{lr}^2}\right) \quad (12)$$

Equations (11) and (12) are implemented in canonical form as shown for the pitch case:

$$\begin{bmatrix} 1 & 0 & 0 \\ 0 & 1 & 0 \\ 0 & -1 & 1 \end{bmatrix} * \begin{bmatrix} (\dot{x}_1)_q \\ (\dot{x}_2)_q \\ \dot{\eta}_{qll} \end{bmatrix} = \begin{bmatrix} 0 & 1 & 0 \\ -\omega_{lr}^2 & -2\zeta_{lr}\omega_{lr} & 0 \\ \omega_q^2 & 2\zeta_q\omega_q & 0 \end{bmatrix} * \begin{bmatrix} (x_1)_q \\ (x_2)_q \\ \eta_{qll} \end{bmatrix} + \begin{bmatrix} 0 \\ 0 \\ 0 \end{bmatrix} + K_q [q] \quad (13)$$

where, $\dot{\eta}_{qll} = q_{lead-lag}$.

A similar setup is used for the roll case, where the regressive lag damping and natural frequency is constrained to that of the pitch case.

Altogether the inclusion of the lead-lag dynamics results in 6 additional states to the model structure. These states are summarized in the state vector shown below.

$$(x)_{lead-lag} = [(x_1)_p \ (x_2)_p \ \eta_{pll} \ (x_1)_q \ (x_2)_q \ \eta_{qll}] \quad (14)$$

Identified Hybrid Model for Hover

The identified parameters in the M-matrix, F-matrix, and G-matrix are presented in Tables 1-3 respectively for the hover flight condition. These tables indicate that the identified parameters have acceptable theoretical accuracy parameters because most Cramer-Rao bounds are less than 20% and most insensitivities are less than 10%. The derivatives M_u , X_u , and N_r were determined outside of the model identification and then fixed in the model structure. M_u was determined based on trim data and then fixed in the model structure. X_u was fixed based on relationship of q/u at low frequency. These methods of determining M_u and X_u are described in Ref. 1. N_r was fixed based on a first order transfer function fit of r/X_P .

The cost functions shown in the Table 4 indicate that the model is an excellent match to the flight identified

frequency responses. An individual cost below 150-200 is considered acceptable, and an average cost below 100 is considered good.

Overlays of the model vs. the flight data in the frequency domain are shown for the on-axis and key off-axis lateral and longitudinal responses in Figs. 6 – 8. The pedal and collective responses showed similar fidelity (as indicated by the cost function in Table 4) but are not pictured herein for brevity.

In order to check the validity of the model, some of the identified parameters were compared against their theoretical values. These validations are shown in the following sections of this paper.

Flapping Constant

The identified value of the flapping constant was checked against the theoretical value:

$$(\tau_f)_{theory} = \left[\frac{\gamma^* \Omega}{16} \left(1 - \frac{8e}{3R} \right) \right]^{-1} \quad (15)$$

where: $\gamma^* = 5.97$ (reduced based on dynamic inflow theory described in Ref. 6).

From the calculations in Eq. (15), the S-76 identified theoretical flap constant is shown to be consistent with theory:

$$(\tau_f)_{theory} = 0.09057 \quad (16)$$

$$(\tau_f)_{ID} = 0.09118 \quad (17)$$

$X_{\beta_{1c}}$ and $Y_{\beta_{1s}}$ Terms

The theoretical value for $X_{\beta_{1c}}$ and $-Y_{\beta_{1s}}$ is the gravity constant (32.17 ft/s²). The identified value was close to gravity at $X_{\beta_{1c}} = -Y_{\beta_{1s}} = 30.28$. These parameters are reasonably consistent with theory considering that the small offset is likely due to uncertainty in the exact location of the vertical center-of-gravity.

Lag-Regressive Mode

The regressive lead-lag dynamics (in the fixed-frame) were identified as a lightly-damped mode ($\zeta_{llr} = 0.121$) with a natural frequency of 25.5 rad/sec ($\omega_{llr} = 25.5$). It is useful to determine the associated value of the lag regressive mode frequency in the rotating frame (ν_ζ).

This identified ν_ζ was evaluated against the theoretical value based on hinge offset.

The lead-lag mode in the fixed-frame is transformed to the rotating frame by shifting the imaginary part of the eigenvalue (damped natural frequency) by the rotor rotational speed (Ω). The real part of the mode is unchanged by the transformation. The equation used to accomplish the transformation is:

$$\nu_\zeta = \sqrt{\frac{(\Omega - \omega_{dllr})^2 + \sigma_{llr}^2}{\Omega^2}} = 0.241 \quad (18)$$

The theoretical value for the lag regressive mode can be calculated using the hinge offset:

$$(\nu_\zeta)_{theoretical} = \sqrt{\frac{3}{2} \left(\frac{e}{1-e} \right)} = 0.24 \quad (19)$$

The excellent agreement between the theoretical and identified values for the rotating lag frequency shows that the lead-lag model was physically meaningful and accurate.

Overall, these checks provided additional confidence in the model by validating that it was physically meaningful. This analysis of the parameter values as well as the theoretical accuracy metrics and the final time domain verification shown in the next section ensure that the model is accurate.

Time Domain Verification for Hover

The model was verified in the time domain to ensure that it could accurately predict the aircraft's motion. The pilot's inputs from flight doublets were used to excite the model, then the model responses and the aircraft responses to this doublet were compared. Note that these data were not used in the model identification process. If the responses matched, then it could be concluded that the model had good predictive accuracy.

The doublet time histories for lateral and longitudinal inputs are shown in Figs. 9 – 10. The plots show that excellent agreement existed between the identified model and the flight test data. Similar model accuracy was observed for the collective and pedal doublet, although they are not shown in this paper.

120 knots Level Flight Model Identification

A second model was identified for a flight condition of 120 knots level flight. Again, frequency domain system identification methods were used. This model identification was also carried out using piloted frequency sweeps of the longitudinal cyclic stick, lateral cyclic stick, collective stick and pedals flown in West Palm Beach, Florida.

Frequency Response Determination

The input signals were the same as the hover model identification. Sideslip and angle of attack were used as additional output signals for the 120kts model. Thus, the output signals were $p, q, r, a_x, a_y, a_z, \dot{u}, \dot{v}, \dot{w}, \alpha$ and β . The velocity derivative signals \dot{u}, \dot{v} and \dot{w} were reconstructed using Eqs. (1) – (3).

Model Structure Determination

Many of the higher order effects modeled in hover tend to wash out in forward flight. To determine which (if any) higher order dynamics were necessary for the 120kts flight condition, the frequency response were inspected similarly to the hover case.

This identified model was to be used in support of S-76D AFCS design. Therefore, it was important that off-axis responses to longitudinal and lateral stick inputs were represented well by the identified model. In addition, the on-axis lateral and longitudinal angular rate responses needed to be accurate at higher frequencies such that the lead-lag dynamics could be properly represented. Consequently, the flap/fuselage dynamics were included in the mode structure. As mentioned earlier, the lag regressive mode is important for AFCS design. Therefore, a representation of the lead-lag dynamics were included in the model structure.

The coherence of the yaw rate response to collective stick frequency response pair was poor. This indicates that in forward flight the yaw response to collective is too small to provide enough information content for accurate identification. Therefore, the engine effect on the yaw rate response from collective was not necessary in the model structure.

Inflow dynamics typically wash out in forward flight. This was true for the S-76 model identification as indicated by the flat trend of the magnitude of the w/X_C frequency response (inflow effects create a rising magnitude curve at higher frequencies). Therefore, the coning-inflow dynamics were not needed in the model structure.

Hybrid Model Structure

This model was identified with flap/fuselage hybrid dynamics for the lateral and longitudinal inputs. Higher-order dynamics were not needed for collective and yaw inputs, as shown in the previous section of this report, and therefore these dynamics were modeled with quasi-steady equations-of-motion. Following these identifications, the lead-lag dynamics were identified as filters on the pitch and roll angular responses.

The equations-of-motion were largely based on those described in Ref. 1. A modification was made to the state equations for the flap/fuselage dynamics. It was found that a yawing moment term due to lateral flapping was necessary to accurately capture the yaw response to lateral stick. Thus, an $N_{\beta_{1s}}$ term was included in the model structure. This modification resulted in the removal of the N_{X_A} derivative to avoid double accounting for the control derivative.

The model structure used for this identification was the same as that presented in Eq. (4) and Eq. (5). The state,

input and output vectors for this model identification are shown below.

$$x = [u \quad v \quad w \quad p \quad q \quad r \quad \phi \quad \theta \quad \beta_{1s} \quad \beta_{1c} \quad (x_1)_p \quad (x_2)_p \quad \eta_{pll} \quad (x_1)_q \quad (x_2)_q \quad \eta_{qll}] \quad (20)$$

$$u = [X_A \quad X_B \quad X_C \quad X_P] \quad (21)$$

$$y = [\dot{u}_m \quad \dot{v}_m \quad \dot{w}_m \quad p \quad q \quad r \quad a_x \quad a_y \quad a_z \quad (a_y)_2 \quad (a_z)_2 \quad \alpha \quad \beta] \quad (22)$$

Identified Hybrid Model

The identified parameters in the F-matrix and G-matrix are presented in Tables 5 - 6. Similar to the hover model identification, these tables indicate that the identified parameters had acceptable theoretical accuracy parameters because most Cramer-Rao bounds were less than 20% and most insensitivities were less than 10%.

The frequency domain costs for this identified model are presented in Table 7. It can be seen that most of the frequency response pairs had cost functions less than or within the acceptable 150-200 range.

As the identification of this case developed, the identification of the Dutch roll mode was a challenge. First, all frequency responses associated with the Dutch roll mode had a loss of coherence around the Dutch roll frequency, which was approximately at 1.5 rad/s. Figure 11 shows an example of this for the \dot{v}/X_P frequency response.

Assuming adequate spectral resolution, low coherence primarily happens for these two reasons:

1. Low signal-to-noise ratio
2. Non-linearity between input and output signals

If the response had a low signal-to-noise ratio at the Dutch-roll frequency, a loss of spectral power around 1.5 rad/sec would be visible in the autospectrum. Figure 12 shows the input, output, and cross spectral densities for the \dot{v}/X_P response. The figure shows that the input autospectrum was fairly level across the Dutch roll mode frequency, with only a small dip around the mode. This indicates that the input was reasonably large in magnitude at the Dutch roll mode frequency and that the loss of coherence was not due to low input signal. In the output autospectrum, it can be seen that the response was large around Dutch roll mode frequency as well. Therefore, this analysis of the autospectra showed that the system was sufficiently excited near the Dutch roll mode frequency, and therefore the loss of coherence was not due to low signal-to-noise ratio.

Since the analysis has shown that the low coherence is not due to #1 above, it must be due to #2, nonlinearity between the input and output signals. Dutch Roll nonlinearity of a helicopter at high speed is discussed in

Chapter 5 of Ref. 7. The reference indicates that this nonlinearity is likely due to tail/empennage interaction with the main rotor wake. Despite the presence of these nonlinear dynamics, the goal was to provide the best possible linear representation of the system. When dynamics are nonlinear, the frequency response as obtained from a Fourier transform is the first harmonic component of a Fourier series, and constitutes the describing function that best characterizes the nonlinear behavior (Ref. 8, Ref. 1). So, the state-space model resulting from frequency response identification is the best linear representation of the nonlinear dynamics.

Model Verification

When the time domain verification of the model was initially performed, it was evident that the model did not predict the damping of the Dutch roll mode correctly. The angular rate response to an initial pedal doublet is shown in Fig. 13. It can be seen in this plot that the identified model predicted too much damping of the Dutch roll mode.

Another difficulty in the verification was due to the nonlinearity observed at the Dutch roll frequency in the previous section of this paper. The verification results from the model confirmed that this motion is nonlinear because of the differences between the Dutch roll mode damping and frequency for two doublets (one right, one left) at the same flight condition. Figure 14 shows that the Dutch-roll mode of the model appears to have a frequency that is lower than flight in the first doublet, and in the second doublet the frequency seems to be higher than flight. This discrepancy shows the presence of nonlinearities because different inputs create varying dynamic characteristics in the response. In the first doublet, we see that the flight response seems to be getting smaller (positive damping ratio) for the first cycles, and then in the last cycle the responses seems to be growing (negative damping ratio). A similar characteristic is shown for high speed Puma Helicopter flight data in Ref. 7, caused by interference effects of the main wake on the tail/empennage. This implies that the Dutch roll mode dynamics of the S-76 are also being affected by the main rotor wake.

Following investigation of the Dutch roll mode, it was necessary to correct the identified model such that the damping of the Dutch roll mode was better represented on average. Ref. 7 provided equations that showed the damping of the Dutch roll mode was largely affected by the N_r derivative.

The N_r derivative was reduced in the identified model until the identified model matched the Dutch roll mode satisfactorily in the time domain. A before/after plot for the angular rate responses to a pedal doublet input is shown in Fig. 15. It can be seen that following the N_r reduction, the identified model predicted the damping of the Dutch roll mode better.

Following the adjustment made to the model for the Dutch roll mode, the model verification was performed. The verification time histories for lateral and pedal are shown in Figs. 16 – 17. The plots show that good agreement existed between the identified model and the flight test data. The longitudinal and collective responses show similar predictive accuracy, but are not shown in the paper for brevity.

GenHel Comparisons

One of the primary design tools for the AFCS design of the S-76D was GenHel (Ref. 9). The GenHel S-76C model is a physics-based nonlinear mathematical model used for prediction of S-76C flight dynamics. In order to improve the GenHel S-76C model, a series of comparisons were performed between the two aforementioned identified models, the S-76C++ flight test data and the GenHel S-76C model. The goal of these comparisons was to find areas in which the GenHel S-76C model was deficient. Two major deficiencies were found:

Off-Axis Responses

A hover longitudinal doublet time history between the flight test data (solid line), the flight test identified model (dashed line) and the GenHel S-76C model (broken dashed line) is shown in Fig. 18. It can be seen that while the flight test identified model matched the flight test data, the GenHel S-76C model was noticeably deficient in predicting the roll rate response to the longitudinal stick doublet input.

A similar comparison was performed for the 120 knots level flight condition and the same conclusion was made. The GenHel S-76C model did not predict the off-axis responses well.

Dutch Roll

Figure 19 shows a pedal doublet at 120 knots level flight in which the flight test data (solid line), the flight test identified model (large dashed line) and the GenHel S-76C model (small dashed line) were compared. It can be seen in the above plot that while the GenHel S-76C model correctly predicted the frequency of the Dutch roll mode, the damping was too high (as was also seen in the original identification results).

GenHel S-76C Model Improvements

As mentioned in the previous section, the GenHel S-76C model did not correctly predict the roll rate response to longitudinal stick inputs. The GenHel S-76C model also did not correctly predict the damping of the Dutch roll mode. A subsequent effort was undertaken to improve the GenHel S-76C model based on these comparisons. The improvements discussed herein will

be the inclusion of aerodynamic phase lag into the model and the inclusion of a destabilizing yaw damping map.

Off-Axis Responses

GenHel has historically been unable to predict off-axis responses to control inputs. Ref. 10 theorized that the reasons for this in different flight regimes was as follows:

1. Hover and low speed flight

The unmodeled effect of geometric wake distortion caused by rotor flapping is the reason for GenHel not correctly predicting the off-axis responses.

2. High speed flight

The 2-D unsteady aerodynamic response associated with the shed wake is the source of the discrepancy between GenHel and flight test data for off-axis responses.

A method that has been used in Ref. 10 to correct this issue is the use of aerodynamic phase lag. Calculation of the aerodynamic forces for each blade element in GenHel is performed using airfoil maps. For a given blade element at a given time, the aerodynamic forces (lift, drag and moment) acting on the blade element are found by using the local angle of attack and Mach number to find the non-dimensional lift, drag and moment coefficients for the blade segment's respective airfoil.

Aerodynamic phase lag manipulates the aerodynamic force lookups for each blade element to cause an effective phase shift in the aerodynamic forcing function on the rotor. The effective phase shift in the aerodynamic forcing function causes the responses to control inputs to be shifted in phase. For longitudinal stick inputs, this phase shift would be most clearly seen in the roll rate response to longitudinal stick input frequency response pair. This is because the roll inertia of the S-76 is significantly less than the pitch inertia. Thus, small changes in the phasing of the aerodynamic forcing function are most notably seen in this off-axis response.

The first step in implementing aerodynamic phase lag was to compare the GenHel S-76C model to flight test data in the frequency domain. This comparison was performed by applying frequency sweeps of the longitudinal stick to the GenHel S-76C model. The data generated from the frequency sweeps was then compared to the longitudinal stick frequency sweeps from the S-76C++ flight test data.

Figure 20 shows the roll rate response to longitudinal stick frequency response pair comparison between the S-76C++ flight test data (solid line) and the GenHel S-76C model (dashed line) for the hover flight condition. It can be seen in the plot that the phase of the GenHel S-

76C model differs significantly from the flight test data for frequencies above 1 rad/s. Also, the magnitude of the GenHel S-76C model is a factor of 4-6 (12-18 dB) less than the test data across all frequencies. This frequency domain comparison were consistent with the GenHel time domain results seen previously in Fig. 18.

Figure 21 below shows the roll rate response to longitudinal stick frequency response pair comparison between the S-76C++ flight test data (solid line) and the GenHel S-76C model (dashed line) for the 120 knot level flight condition. It can be seen in the plot that the phase of the GenHel S-76C model is similar to the test data across all frequencies. However, the magnitude was a factor of 4-8 times less in the GenHel S-76C model when compared to the test data.

To improve the off-axis response in hover, a range of aerodynamic phase lag settings were tested. These phase lags ranged from 10 to 50 degrees in increments of 10 degrees. For each aerodynamic phase lag angle, frequency sweeps of the longitudinal stick were applied to the GenHel S-76C model in hover. The GenHel data for all the angles was then collected and overlaid with the test data. Following this comparison, it was found that 40 degrees of aerodynamic phase lag provided the most improvement in magnitude and phase for the hover flight condition.

A comparison plot of the flight test data (solid line), GenHel S-76C model without aerodynamic phase lag (dashed line) and the GenHel S-76C model with 40 degrees of aerodynamic phase lag (broken dashed line) for the roll rate response to longitudinal stick frequency response pair is shown in Fig. 22. It can be seen that the phase was significantly improved with the use of 40 degrees of aerodynamic phase lag in hover. While the magnitude was improved, it was still 2-4 times less than the flight test data.

The frequency domain comparisons showed that the roll rate response to longitudinal stick was improved in hover for the GenHel S-76C model with the inclusion of 40 degrees of aerodynamic phase lag. It was important to verify these improvements by performing time domain comparisons between the GenHel S-76C model and flight test data. A time history comparison showing the pitch rate and roll rate responses to a longitudinal stick doublet is shown in Fig. 23. It can be seen in the plot that the frequency domain results were confirmed in the time domain. The phase of the off-axis response was significantly improved and a small improvement in magnitude also occurred.

The approach used in hover was also used in an attempt to improve off-axis responses in the GenHel S-76C model at high speed (i.e. 120 knots). Aerodynamic phase lag between 10 and 30 degrees in increments of 10 degrees were put into the GenHel S-76C model. For each increment, frequency sweeps of the longitudinal stick were performed with the GenHel S-76C model.

The data was then collected and compared to the flight test data. Following this comparison, it was found that 20 degrees of aerodynamic phase lag produced the most improvement in the roll rate response to longitudinal stick frequency response pair. The reduction in aerodynamic phase with airspeed is also indicated for the helicopters in Ref. 10.

A comparison plot of the roll rate to longitudinal stick frequency response pairs for the flight test data (solid line), GenHel S-76C model without aerodynamic phase lag (dashed line) and the GenHel S-76C model with 20 degrees aerodynamic phase lag (broken dashed line) at 120 knots is presented in Fig. 24. The plot showed that the phase improvement was minimal and while the magnitude improved significantly at lower frequencies, it was worse than the model without aerodynamic phase lag at higher frequencies.

A time domain comparison was performed at 120 knots to check the frequency domain results. Figure 25 presents a plot of pitch rate and roll rate vs. time for a longitudinal stick doublet at 120 knots. It can be seen that the inclusion of 20 degrees aerodynamic phase lag had no significant effect on the roll rate response to longitudinal stick. This result was consistent with the minimal improvement seen in the frequency domain at 120 knots.

Complete implementation of aerodynamic phase lag in a GenHel model requires multiple data points. Unfortunately, the S-76C flight test data was limited and the determinations of aerodynamic phase lag at hover and 120 knots were all that could be performed. However, Ref. 9 stated that experience has shown that aerodynamic phase lag is typically highest in hover and then “washes out” with increasing airspeed. Therefore, an approach was taken to use the two S-76C data points; hover and 120 knots, and generate a map that washes out from hover to 120 knots. The resulting aerodynamic phase lag map as a function of rotor advance ratio for the GenHel S-76C model is plotted in Fig. 26.

Dutch Roll

The comparison plots between the GenHel S-76C model and flight test data at 120 knots showed that while the GenHel S-76C model accurately predicted the frequency of the Dutch roll mode, the damping of the Dutch roll mode was too high. This relationship between the GenHel S-76C model and the test data was very similar to that seen between the flight test identified model and the test data. Because of this similarity, the same corrective action used for the identified model was attempted with the GenHel S-76C model (i.e. reduce the yaw damping).

Adjustment of the yaw damping was achieved by placing a destabilizing yaw moment map within the fuselage module of the GenHel S-76C model. This was

the selected location of the correction for the following two reasons:

1. The module already existed within GenHel S-76C model for the fuselage force and moment maps
2. The fuselage module accepts non-dimensional force and moment parameters thereby scaling parameters appropriately with changes in ambient conditions

The yaw damping map accepted yaw rate and output non-dimensional yawing moment in ft^3 . Determination of the map was performed through observation of the Dutch roll mode eigenvalue damping and time domain comparisons between the GenHel S-76C model and flight test data.

The first flight condition for which the yaw damping map was determined was 120 knots level flight. The yaw damping map determined for this flight condition is presented in Fig. 27. It can be seen that the map was destabilizing in that a positive yaw rate resulted in a positive yawing moment.

It was useful to compare the level of yaw destabilization required in the GenHel S-76C model at this flight condition to that required in the flight test identified model for the same flight condition. For the GenHel S-76C model, the reduction in N_r caused by using the yaw damping map to achieve better Dutch roll mode correlation was 0.74. The reduction in N_r for the flight test identified model at the same flight condition for good Dutch roll mode correlation was 0.55. Through this comparison it was concluded that the N_r reductions required for both models to predict the Dutch roll mode well were comparable to one another.

A time domain comparison between the flight test data, the GenHel S-76C model without the yaw damping map and the GenHel S-76C model with the yaw damping map for a pedal doublet at 120 knots is shown in Fig. 28. It can be seen that the use of the yaw damping map leads to a better representation of the Dutch roll mode when compared to flight test data.

The damping of the Dutch roll mode for the S-76 changes with airspeed. Therefore, it was necessary to make the yaw damping map a function of forward flight airspeed as well. This required additional flight conditions be examined to determine the values required in the yaw damping map. Test data was available for an 80 knots level flight condition. Therefore, this was the next condition assessed.

Figure 29 shows a time domain comparison between the GenHel S-76C model without the yaw damping map (i.e. yaw damping map was zero) and flight test data at 80 knots level flight for a pedal doublet input. The plot shows that the model was fairly good in representing the frequency and damping of the Dutch roll mode at this flight condition. Therefore, it was concluded that no yaw damping map was necessary at 80 knots.

Speeds above 120 knots were not tested during the S-76C++ flight test program for safety of flight concerns. Therefore, it was necessary to use previous S-76 test data to estimate the damping of the Dutch roll mode at higher flight speeds. This estimate of damping was then to be used as a basis for choosing the yaw damping map for higher airspeeds in the GenHel S-76C model.

Pedal pulse data at 150 knots was collected during an S-76A flight test program conducted in 1977. Unfortunately, this test data was not available in an electronic format. Therefore, a visual assessment of the test data was made and it was estimated that the damping ratio of the S-76 Dutch roll mode at 160 knots was approximately -0.1. Because no time domain comparisons could be performed at higher speeds, the yaw damping map was adjusted until the damping ratio of the Dutch roll mode in the GenHel S-76C model was near -0.1 at higher airspeeds.

Altogether, yaw damping maps were determined at 80 knots, 120 knots and 160 knots. These maps were combined to form the yaw damping map for the GenHel S-76C model. The yaw damping maps determined for the GenHel S-76C model at 80 and 160 knots are presented in Fig. 30.

Since the yaw damping maps were defined for three specific airspeeds, linear interpolation within the GenHel software was used to determine the yaw damping maps for other airspeeds. Because of this interpolation, it was necessary to check that the progression of the Dutch roll mode eigenvalues with airspeed was sensible (i.e. smooth variation with airspeed). To perform this check, linear models were extracted from the GenHel S-76C model for speeds from 80 to 160 knots in increments of 10 knots. The eigenvalues for each condition were then overlaid with one another such that a locus of the Dutch roll mode eigenvalues with airspeed was clear. This plot is presented in Fig. 31. It can be seen in the plot that the progression of the Dutch roll mode eigenvalues was smooth from 80 – 160 knots. Therefore, it could be concluded that the inclusion of the yaw damping map achieved the desired objective of improving the GenHel S-76C model's ability to predict the damping of the Dutch roll mode.

Conclusions/Recommendations

System identification of two flight conditions, hover and 120 knots, were successfully completed using frequency domain system identification methods. The resulting linear models provided physically meaningful models that were used to correct the S-76C GenHel nonlinear math model. A summary of lessons learned from this effort are:

1. CIFER[®] frequency domain identification process was an efficient and effective method for identifying linear models with complex hybrid model architecture.
2. The identification hybrid model parameters agreed well with theoretical values thus indicating physical meaningfulness.
3. The use of aero-phase lag corrections and yaw damping maps provided improvements in S-76C GenHel model correlation to flight data.

Following the completion of the S-76C model identification and simulation correlation a series of recommendations for future work have been made. These recommendations are summarized below:

1. The S-76 Dutch roll mode was difficult for both the identified model and the GenHel S-76C model to predict. During S-76D flight testing, a dedicated number of runs should be performed to better understand the physical origin of the S-76 Dutch roll mode.
2. The model identification process had difficulty identifying the damping of the Dutch roll mode. This issue should be investigated to determine if there are better solutions other than those employed during the S-76C model identifications (i.e. manually adjusting parameters).
3. The magnitude of the roll rate response to longitudinal stick inputs was improved but only to a certain point with the use of aerodynamic phase lag. Additional approaches (e.g. inflow modeling) should be explored to see if it is possible for the GenHel S-76C model to better predict these off-axis responses.

Acknowledgments

C. Quiding thanks J. Sleight, W. Boyce, D. Boulos, S. Ruiz, N. Brinkmeier, T. Davis and other members of the Sikorsky Flight Test Engineering and Instrumentation Engineering organizations for their efforts in configuring and flight testing the S-76C++ test aircraft. C. Quiding also thanks J. Howlett, J. Sola, O. Wulff, P. Berestesky, S. Wright and AFDD for their assistance in reducing and analyzing the flight test data.

References

- ¹ Tischler, M. B. and Remple, R. K., Aircraft and Rotorcraft System Identification: Engineering Methods With Flight Test Examples, AIAA Aug 2006.
- ² Fletcher, Jay W; Tischler, Mark B, "Improving helicopter flight mechanics models with laser measurements of blade flapping", AHS, Annual Forum, 53rd, Virginia Beach, VA; UNITED STATES; 29 Apr.-1 May 1997. pp. 1467-1494. 1997.
- ³ Tischler, Mark B, Cauffman, Mavis G, "Frequency Response method for rotorcraft system identification identification with applications to the BO-105

helicopter”, AHS, Annual Forum, 46th, Washington, DC; UNITED STATES; 21-23 May 1990. pp. 99-137. 1990.

⁴ Harding, Jeff, Moody, Scott, “Identification of AH-64D Dynamics to Support Flight Control System Evaluations,” Proceedings of the American Helicopter Society 61st Annual Forum, Grapevine, Texas, June 1-3 2005.

⁵ Christensen, K. T., Campbell, K. G., Griffith, C. D., Ivler, C. M., Tishcler, M. B., Harding, J. W., “Flight Control Development for the ARH-70 Armed Reconnaissance Helicopter Program”, American Helicopter Society 63rd Annual Forum, Virginia Beach, VA, May 1-3, 2007.

⁶ Curtiss, H.C., Jr., “Stability and Control Modeling,” Vertica, Vol. 13, No. 3, 1989, pp. 229-250.

⁷ Padfield, Gareth D., “Helicopter Flight Dynamics: The Theory and Application of Flying Qualities and Simulation Modeling,” Virginia and Oxford: AIAA and Blackwell, 1999, pp. 246-247.

⁸ Ogata, Katsuhiko, “Modern Control Engineering,” Prentice-Hall Inc., Englewood Cliffs, NJ, 1970, pp. 538-553.

⁹ Howlett, J. J., "UH-60A Black Hawk Engineering Simulation Program: Volume I - Mathematical Model," NASA CR-166309, December 1981.

¹⁰ Tischler, M.B. and Mansur, M.H., “An Empirical Correction for Improving Off-Axes Response in Flight Mechanics Helicopter”, Journal of the American Helicopter Society, Vol. 43, no. 2, April 1998, pp. 94-102.



Figure 1. S-76D Helicopter

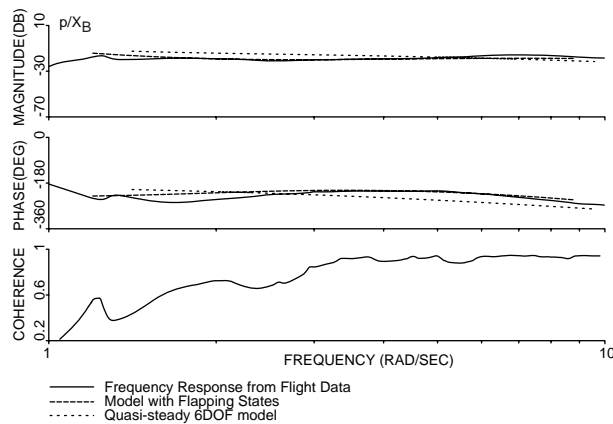


Figure 2. Example comparison of p/X_B for 6DOF and hybrid models vs. flight data at hover.

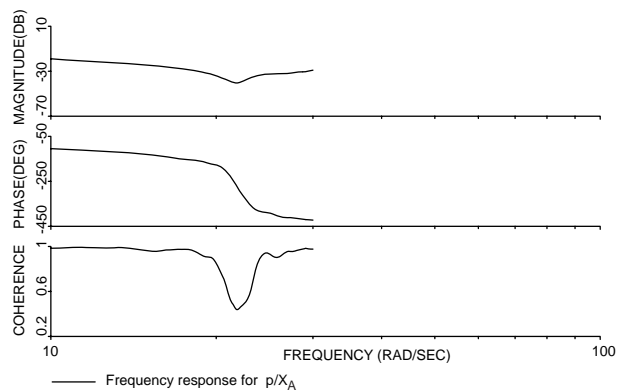


Figure 3. Frequency response for p/X_A in the frequency range of the lag-regressive mode at hover.

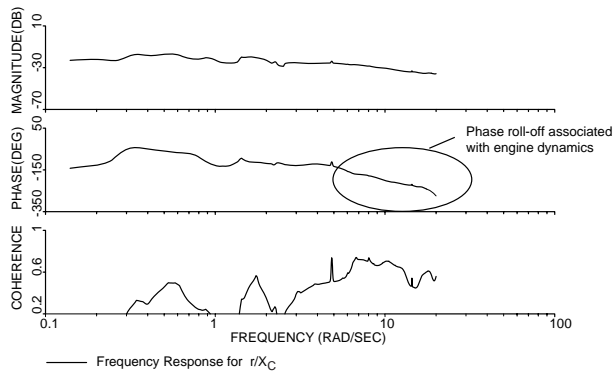


Figure 4. Effect of engine dynamics on the yaw response to collective (r/X_C) at hover.

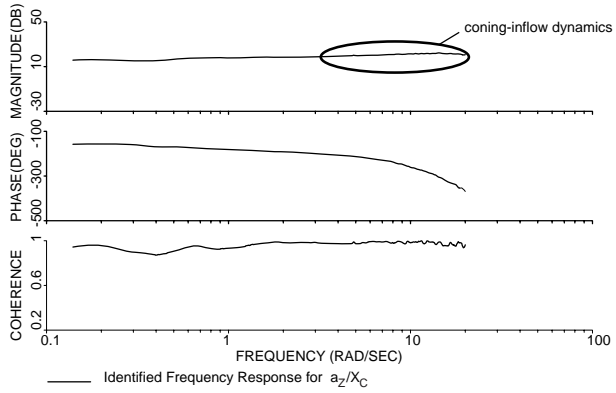


Figure 5. Effect of inflow dynamics on the vertical acceleration response to collective (a_z/X_C) at hover.

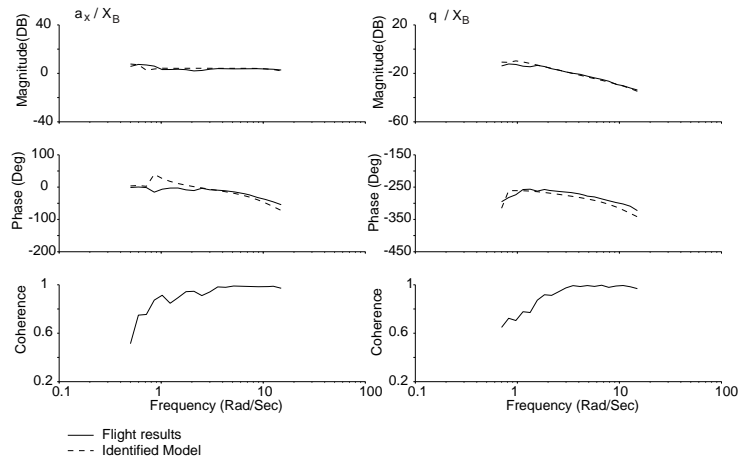


Figure 6. Model vs. flight data for on-axis longitudinal responses at hover (a_x/X_B and q/X_B).

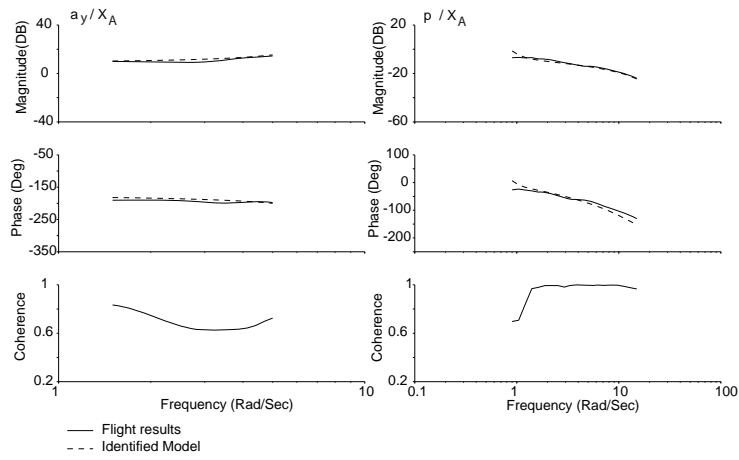


Figure 7. Model vs. flight data for on-axis lateral responses at hover (a_y/X_A and p/X_A).

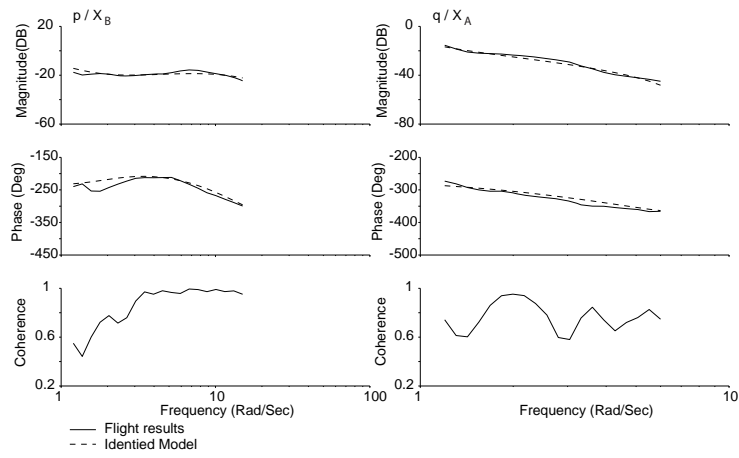


Figure 8. Model vs. flight data for key off-axis responses at hover (p/X_B and q/X_A).

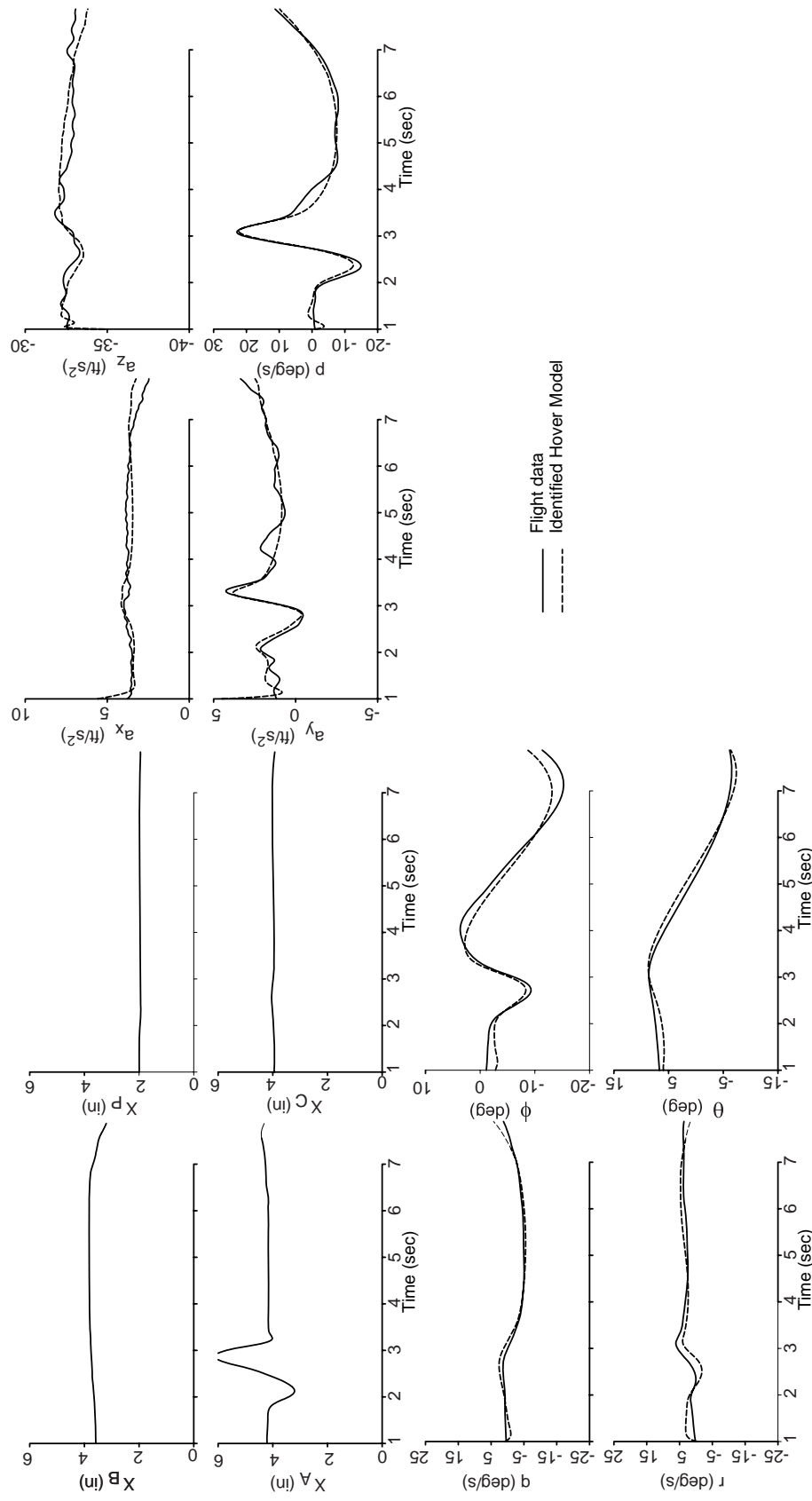


Figure 9. Time domain verification at hover for a lateral doublet.

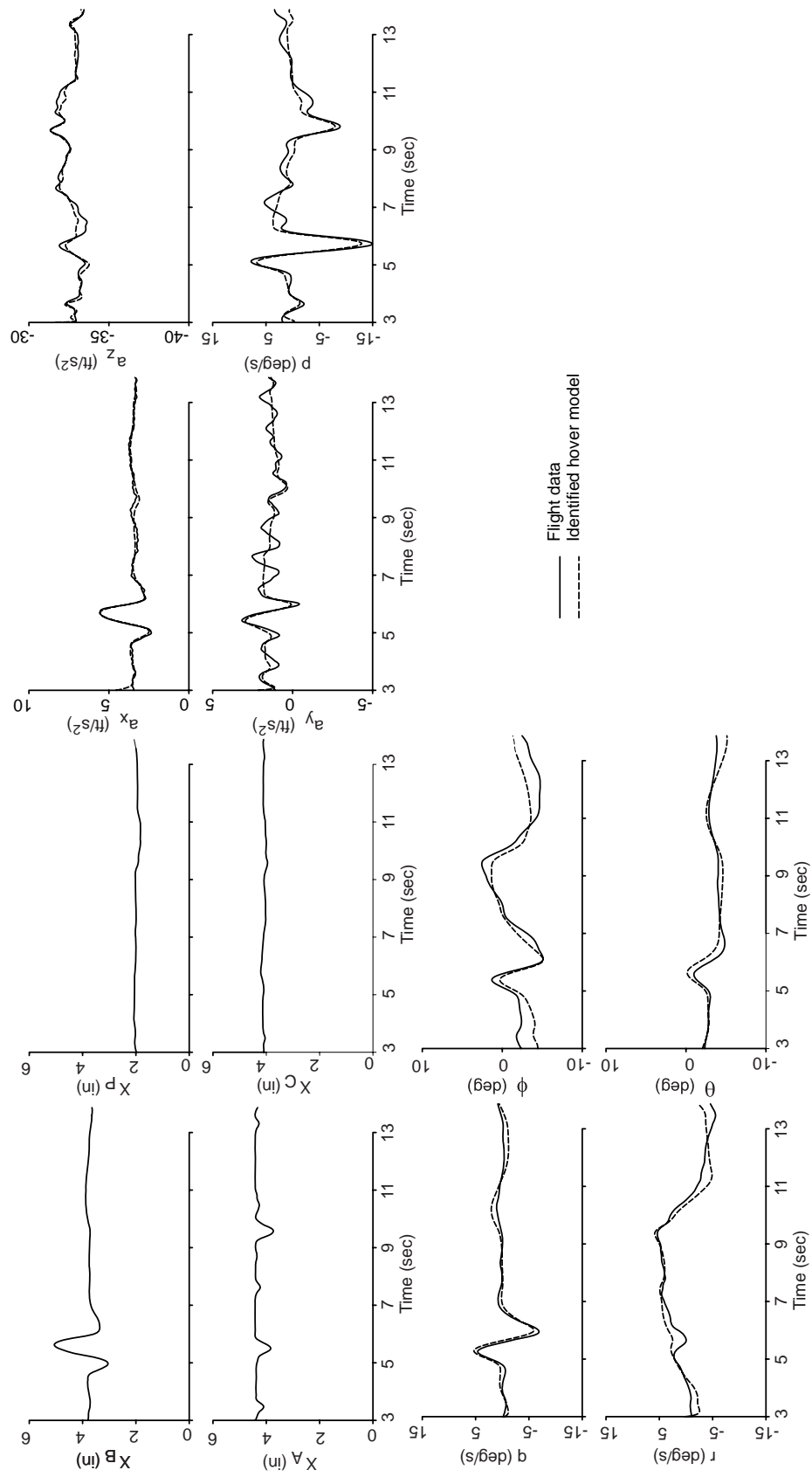


Figure 10. Time domain verification at hover for a Figure

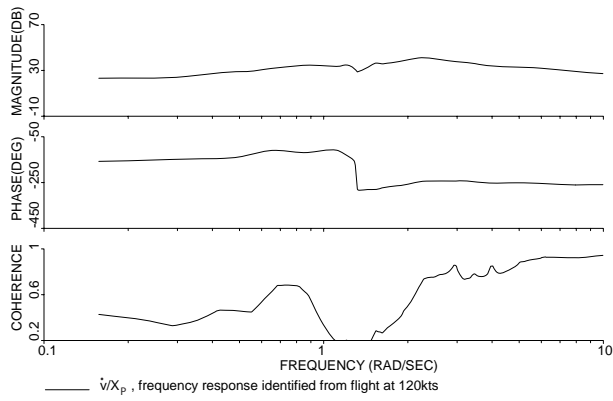


Figure 11. Pedal to lateral velocity response (\dot{v}/δ_{ped}) at 120 knots.

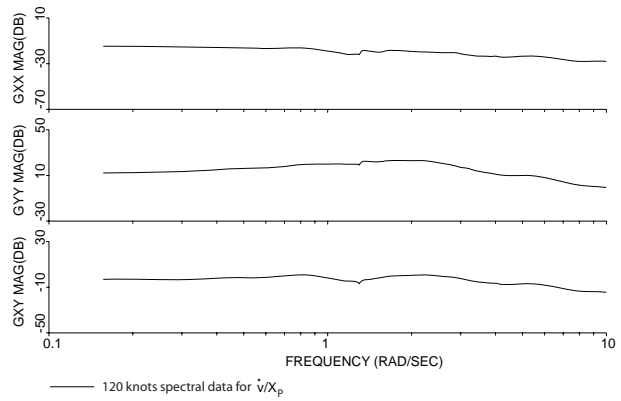


Figure 12. Spectral data for pedal to lateral velocity response (\dot{v}/δ_{ped}) at 120 knots.

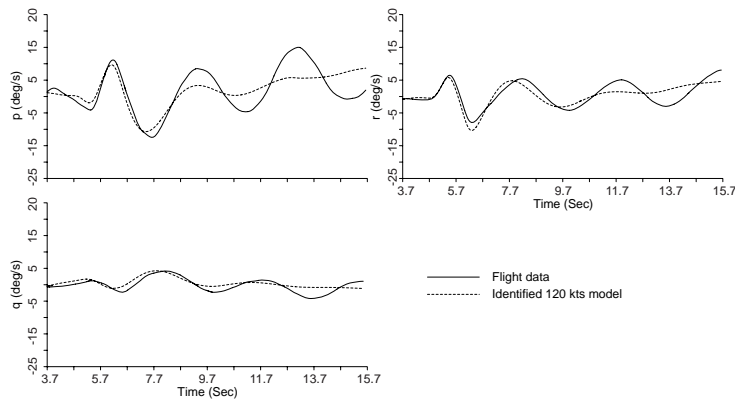


Figure 13. Angular rate responses to pedal doublet input at 120 knots.

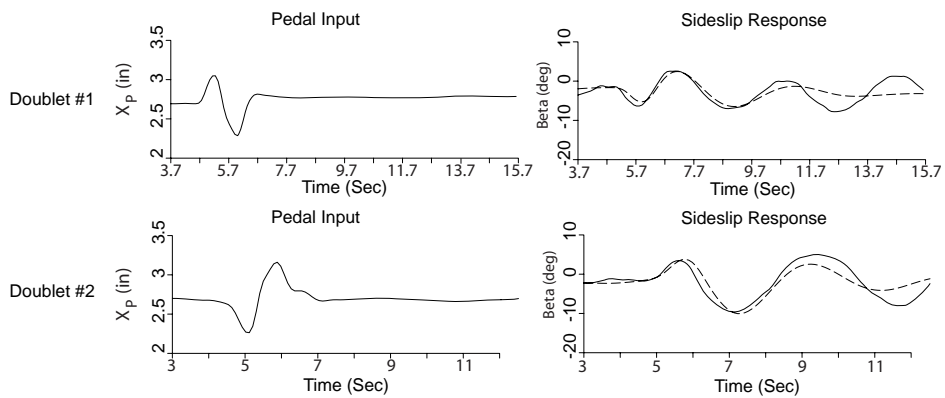


Figure 14. Comparison of positive and negative pedal doublets at 120 knots.

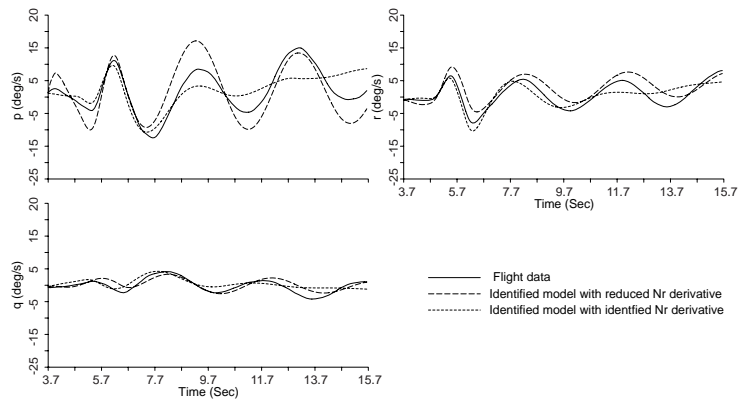


Figure 15. Effect of adjusting N_r on Dutch roll mode.

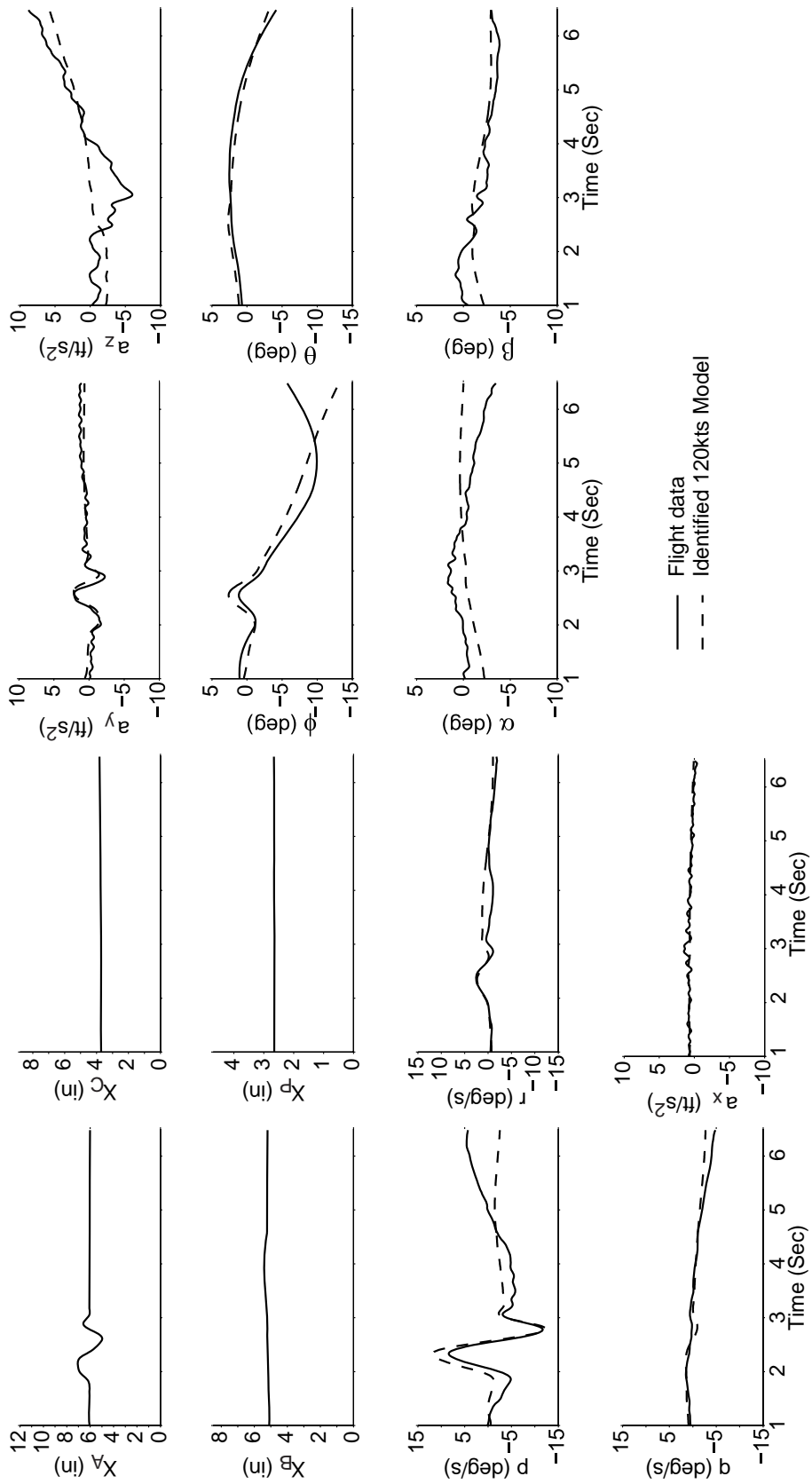


Figure 16. Time domain verification for 120 knots level flight lateral doublet.

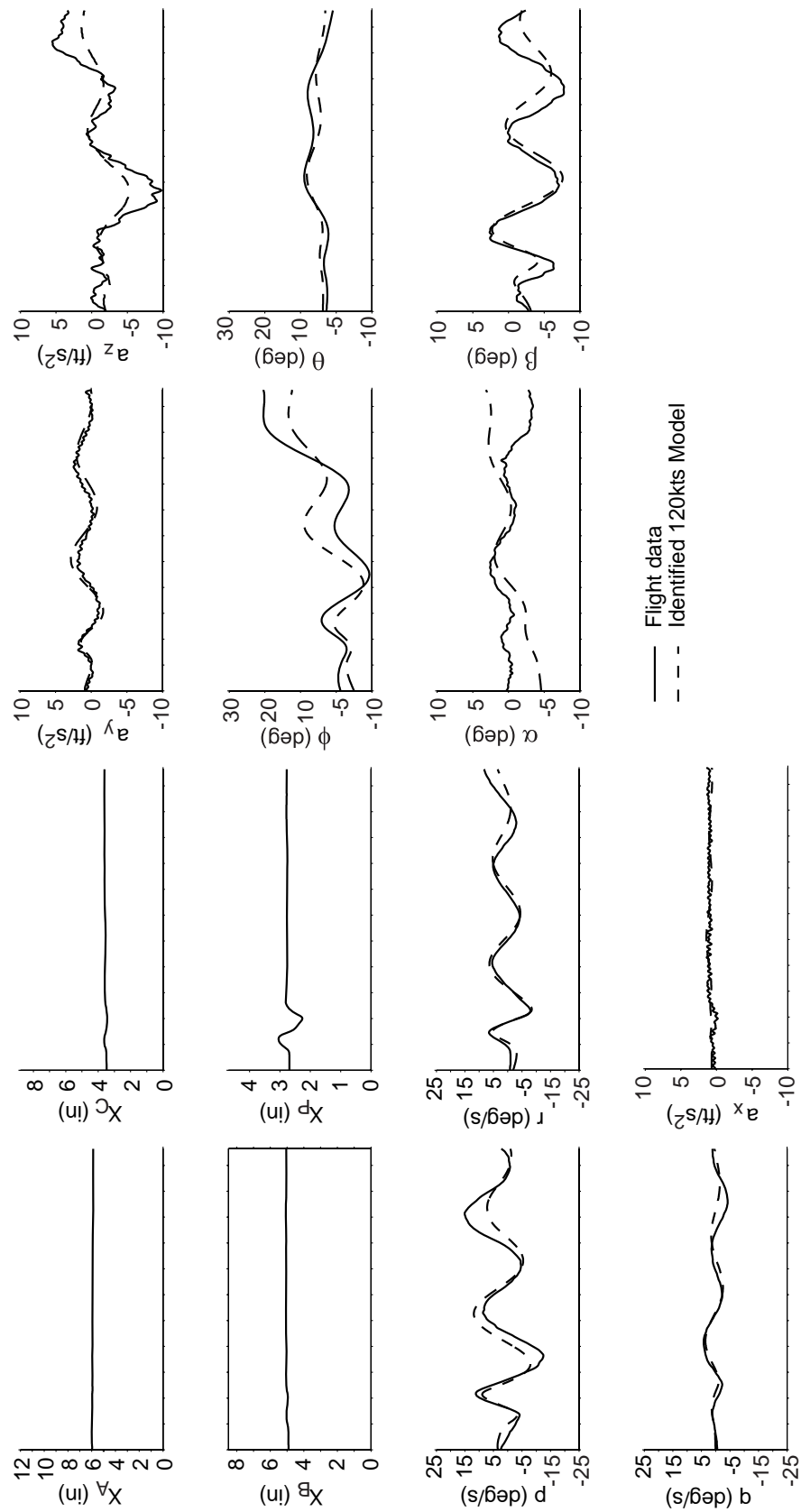


Figure 17. Time domain verification for 120 knots level flight pedal doublet.

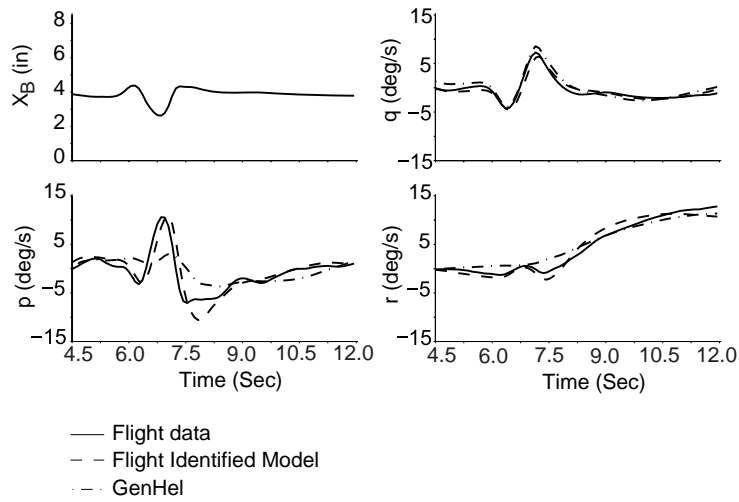


Figure 18. Hover longitudinal response comparisons between flight data, the flight identified model, and GenHel.

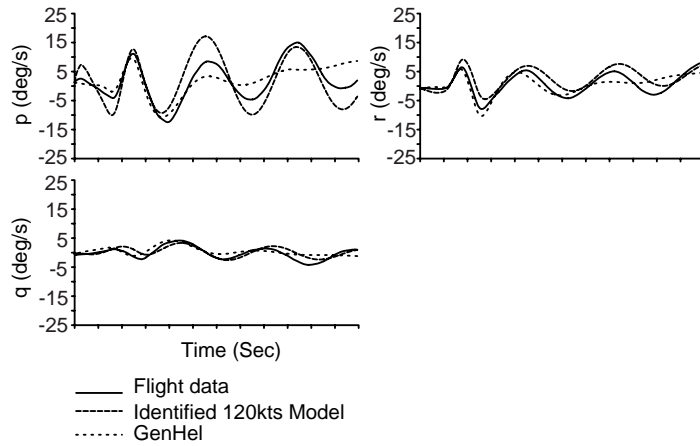


Figure 19. 120kts pedal response comparisons between flight data, the flight identified model, and GenHel

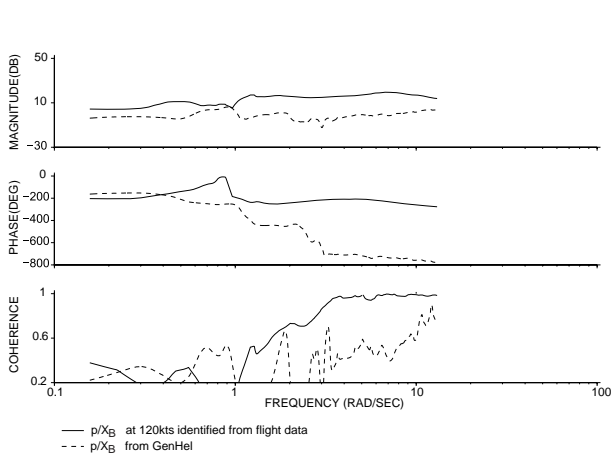


Figure 20. p/X_B S-76C flight test to GenHel S-76C at hover.

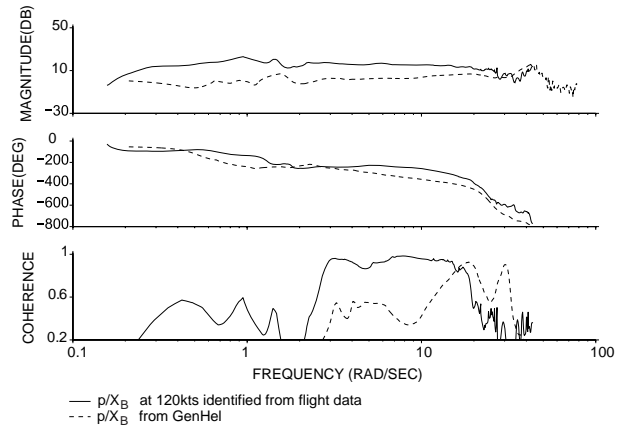


Figure 21. p/X_B S-76C flight test to GenHel S-76C at 120 kts.

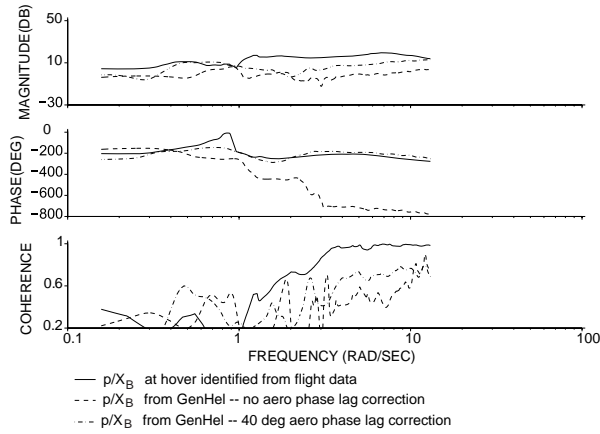


Figure 22. p/X_B S-76C flight test GenHel S-76C w/o aero phase lag and GenHel S-76C w/ 40 deg. aero phase lag at hover.

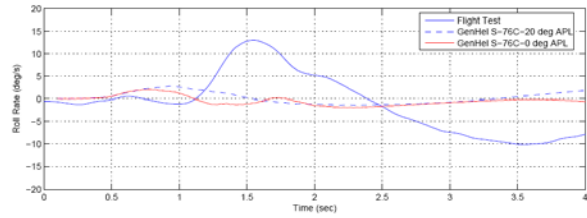
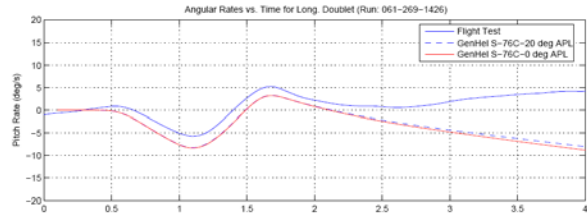


Figure 25. Pitch and roll rate vs. time for longitudinal stick doublet at 120 kts.

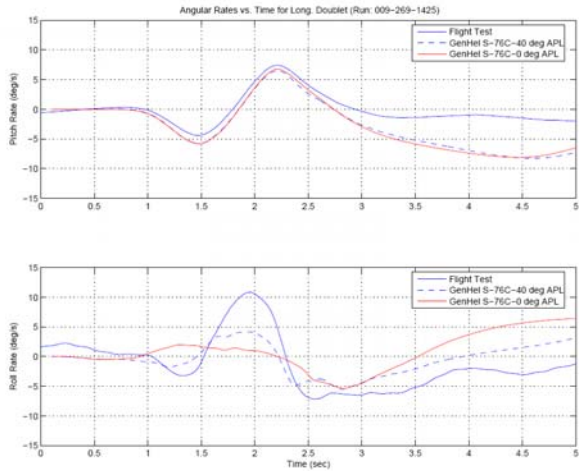


Figure 23. Pitch and roll rate vs. time for longitudinal stick doublet at hover.

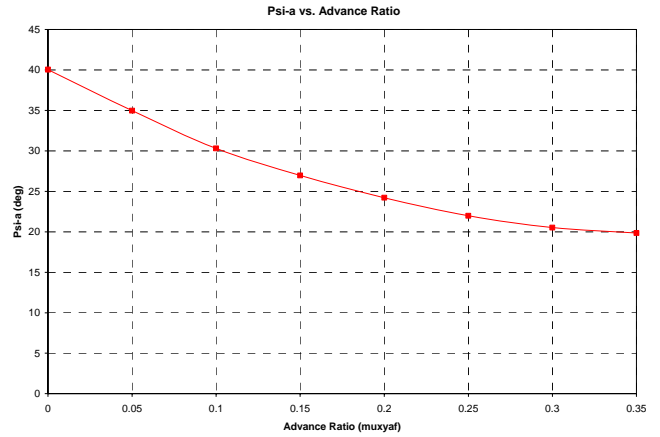


Figure 26. GenHel S-76C aerodynamic phase lag map.

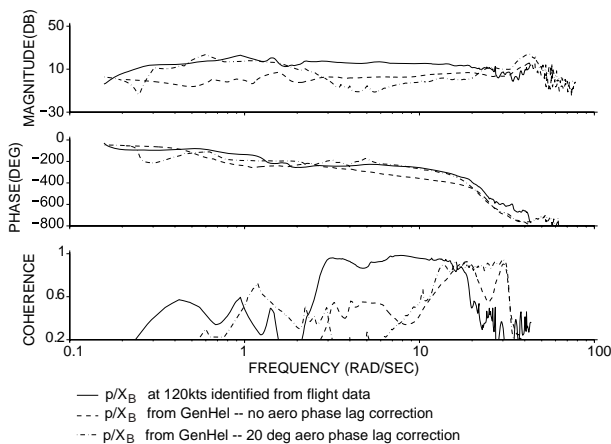


Figure 24. p/X_B S-76C flight test (solid line), GenHel S-76C w/o aero phase lag (dashed line) and GenHel S-76C w/ 20 deg. aero phase lag at 120 kts.

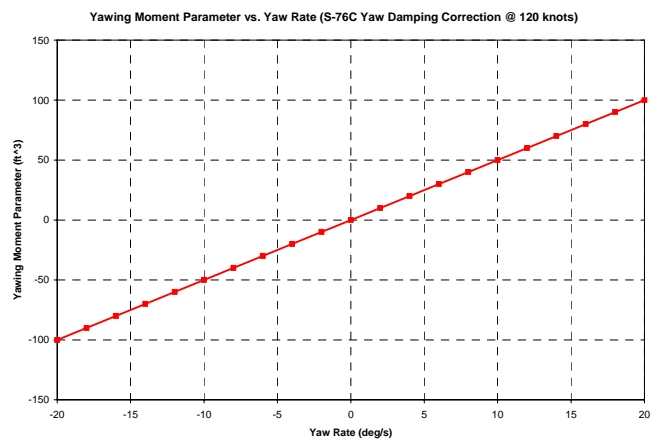


Figure 27. GenHel S-76C yaw damping map at 120 kts.

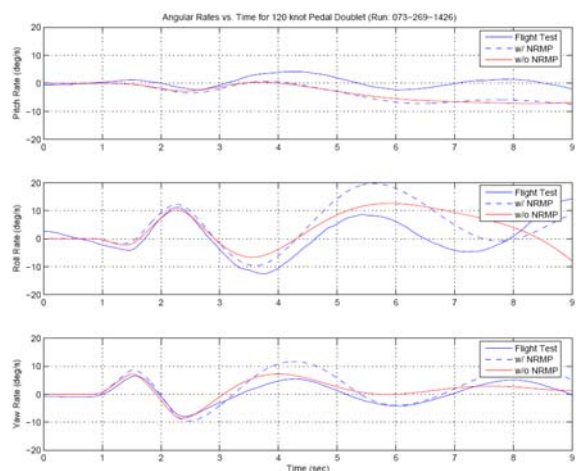


Figure 28. Pitch rate, roll rate and yaw rate vs. time for pedal doublet at 120 kts.

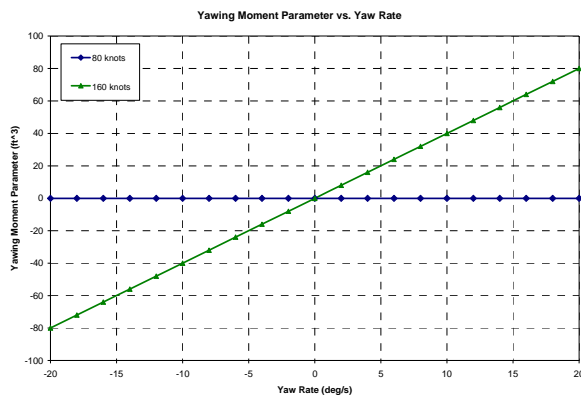


Figure 30. GenHel S-76C yaw damping map at 80 and 160 knots.

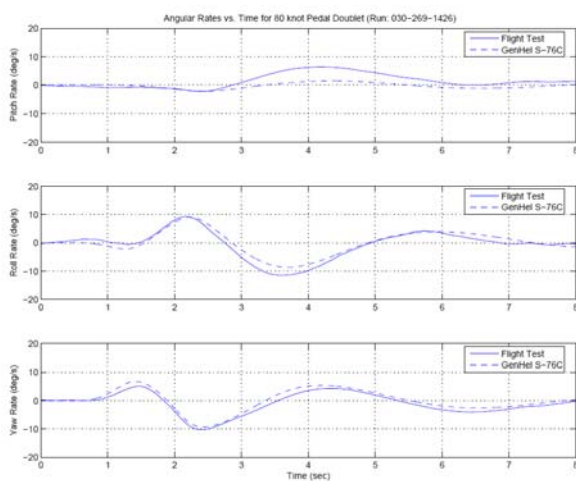


Figure 29. Pitch rate, roll rate and yaw rate vs. time for pedal doublet at 80 kts.

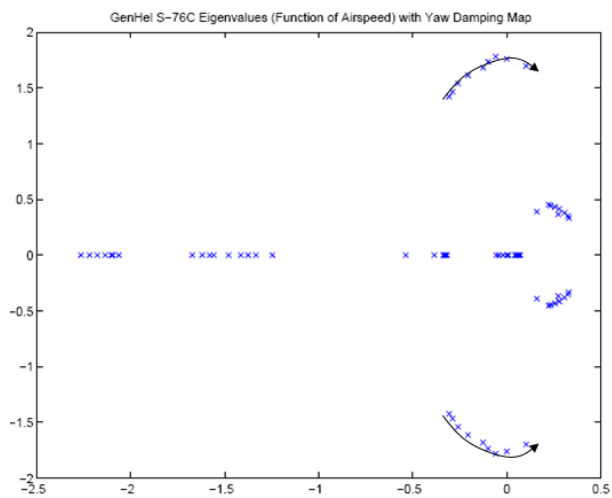


Figure 31. GenHel S-76C Dutch roll mode eigenvalue locii.

Table 1. Identified M-matrix parameters for hover model.

Derivative	Value	Cramer Rao (%)	Insensitivity (%)
$-N_{X_C}$	-0.2724	4.957	2.417
Z_{accel}	2.1	4.413	1.160
τ_{engine}	0.1263	9.505	3.952

Table 2. Identified F-matrix parameters for hover model.

Derivative	Hover	Cramer Rao (%)	Insensitivity (%)
X_u	-0.014 ^a	n/a	n/a
X_v	0 ^b	n/a	n/a
X_w	0 ^b	n/a	n/a
X_r	0 ^b	n/a	n/a
$X_{\beta_{1c}}$	30.28	7.962	0.7008
Y_u	0 ^b	n/a	n/a
Y_v	-0.2113	6.374	1.617
Y_w	0 ^b	n/a	n/a
Y_p	1.101	25.67	10.23
Y_r	0.5869	37.93	9.648
$Y_{\beta_{1s}}$	-30.28 ^c	n/a	n/a
Z_u	0 ^b	n/a	n/a
Z_v	0 ^b	n/a	n/a
Z_w	-0.04383	42.13	17.53
Z_p	0 ^b	n/a	n/a
Z_q	-6.159	9.031	3.30
Z_r	2.398	7.364	2.204
L_u	0 ^b	n/a	n/a
L_v	-0.0620	4.493	0.8579
L_w	0 ^b	n/a	n/a
L_r	0.1388	32.59	8.172
$L_{\beta_{1s}}$	-57.09	4.881	0.6061
M_u	0.01170 ^a	n/a	n/a
M_v	0 ^b	n/a	n/a
M_w	0 ^b	n/a	n/a
M_r	0 ^b	n/a	n/a
$M_{\beta_{1c}}$	-4.472	7.436	0.8747
N_u	0 ^b	n/a	n/a
N_v	0.01387	15.37	4.513
N_w	0 ^b	n/a	n/a
N_p	0 ^b	n/a	n/a
N_q	0 ^b	n/a	n/a
N_r	-0.1830 ^a	n/a	n/a
τ_f	0.09118	4.545	0.7415
$Lf_{\beta_{1c}}$	-0.3371	9.344	0.7415
$Mf_{\beta_{1s}}$	1.318	10.31	1.367
$v_{\hat{\beta}}$	-195.5	6.01981	3.193
K_p	1.410	2.864	0.9987
ω_p^2	502.2	1.130	0.4860
$2\zeta_p\omega_p$	-2.168	11.84	5.725

$-\omega_{ll_r}^2$	-651.9	1.241	0.4622
$-2\xi_{ll_r}\omega_{ll_r}$	-6.159	5.339	2.298
K_q	1.440	3.175	1.153
ω_q^2	503.8	1.100	0.4981
$2\zeta_q\omega_q$	-2.749	9.338	4.411
$-\omega_{ll_{r2}}^2$	-651.9 ^c	n/a	n/a
$-2\xi_{ll_{r2}}\omega_{ll_{r2}}$	-6.159 ^c	n/a	n/a

^aFixed in model structure.

^bEliminated during model structure determination.

^cFixed derivative tied to free derivative $Y_{\beta_{1s}} = -1 * X_{\beta_{1c}} - \omega_{ll_{r2}}^2 = 1.00 * -\omega_{ll_r}^2$, $-2\xi_{ll_{r2}}\omega_{ll_{r2}} = 1.00 * -2\xi_{ll_r}\omega_{ll_r}$

Table 3. Identified G-matrix parameters for hover model.

Derivative	Value	Cramer Rao (%)	Insensitivity (%)
X_{X_P}	0 ^b	n/a	n/a
X_{X_C}	1.292	2.937	1.468
Y_{X_P}	0 ^b	n/a	n/a
Y_{X_C}	0 ^b	n/a	n/a
Z_{X_B}	0.6727	4.674	2.285
Z_{X_A}	0 ^b	n/a	n/a
Z_{X_P}	-1.664	6.618	2.845
L_{X_P}	-0.6572	3.827	1.422
L_{X_C}	0 ^b	n/a	n/a
M_{X_P}	0 ^b	n/a	n/a
M_{X_C}	0 ^b	n/a	n/a
N_{X_B}	0 ^b	n/a	n/a
N_{X_A}	0.1512	3.802	1.898
N_{X_P}	0.8292	4.151	1.398
Lf_{X_B}	0.03498	6.011	0.7578
Lf_{X_A}	-0.01855	5.672	1.215
Mf_{X_B}	0.07530	8.033	0.8493
Mf_{X_A}	0.02572	9.607	1.433
v_{X_C}	49.18 ^c	n/a	n/a
$\dot{\beta}_{X_C}$	30.60	3.754	1.801
τ_{X_B}	0.0 ^b	n/a	n/a
τ_{X_A}	0.0 ^b	n/a	n/a
τ_{X_P}	0.02804	26.30	12.42
τ_{X_C}	0.07162	7.525	3.127

^aFixed in model structure.

^bEliminated during model structure determination.

^cFixed derivative tied to free derivative $v_{\delta_{col}} = 1.607 * \dot{\beta}_{\delta_{col}}$.

Table 4. Cost functions for hover model.

Transfer Function	Cost
\dot{u}/X_B	47.383
p/X_B	84.46
q/X_B	83.157
a_x/X_B	124.340
a_z/X_B	149.784
\dot{v}/X_A	132.847
p/X_A	87.137
q/X_A	56.919
r/X_A	224.027
a_y/X_A	31.810
$(a_y)_2/X_A$	123.294
\dot{v}/X_P	26.947
p/X_P	71.222
r/X_P	129.88
a_z/X_P	155.966
\dot{u}/X_C	50.260
r/X_C	27.928
a_x/X_C	40.084
a_z/X_C	47.869
Average	89.227

Table 5. Identified F-matrix parameters for 120 knots model.

Derivative	Value	Cramer Rao (%)	Insensitivity (%)
X_u	-0.0457 ^a	n/a	n/a
X_v	0 ^b	n/a	n/a
X_w	0.0365	10.02	4.165
X_r	0 ^b	n/a	n/a
$X_{\beta_{1c}}$	40.54	4.255	0.998
Y_u	0 ^b	n/a	n/a
Y_v	-0.3441	5.716	0.805
Y_w	0 ^b	n/a	n/a
Y_p	-7.047	5.969	1.512
Y_r	-3.417	38.88	8.083
$Y_{\beta_{1s}}$	-40.54 ^c	n/a	n/a
Z_u	0.2561	15.47	2.531
Z_v	0 ^b	n/a	n/a
Z_w	-0.3268	5.398	1.106
Z_p	0 ^b	n/a	n/a
Z_q	-48.44	5.257	1.993

Z_r	0 ^b	n/a	n/a
L_u	0 ^b	n/a	n/a
L_v	-0.078 ^a	n/a	n/a
L_w	0.0065	8.896	2.761
L_r	-2.173	15.53	2.867
$L_{\beta_{1s}}$	-62.55	3.143	0.5156
M_u	-0.0035	17.37	2.914
M_v	0 ^b	n/a	n/a
M_w	0.0065	5.68	0.8366
M_r	0 ^b	n/a	n/a
$M_{\beta_{1c}}$	-12.35	4.269	0.6264
N_u	0 ^b	n/a	n/a
N_v	0.0041	15.69	3.551
N_w	0 ^b	n/a	n/a
N_p	0.2233	9.558	2.3
N_q	-0.1611	8.373	2.03
N_r	-0.3 ^a	n/a	n/a
$N_{\beta_{1s}}$	-9.252	4.871	0.8439
$N_{\beta_{1c}}$	1.589	8.274	2.309
τ_f	0.09916	2.803	0.7471
$Lf_{\beta_{1c}}$	-0.506	6.919	0.9594
$Mf_{\beta_{1s}}$	0.528	8.119	1.94
K_p	1.352 ^a	n/a	n/a
ω_p^2	552.2 ^a	n/a	n/a
$2\zeta_p\omega_p$	3.008 ^a	n/a	n/a
$-\omega_{ll_r}^2$	-651.9 ^a	n/a	n/a
$-2\zeta_{ll_r}\omega_{ll_r}$	-6.128 ^a	n/a	n/a
K_q	0.85 ^a	n/a	n/a
ω_q^2	700.0 ^a	n/a	n/a
$2\zeta_q\omega_q$	4.127 ^a	n/a	n/a
$-\omega_{ll_{r2}}^2$	-651.9 ^c	n/a	n/a
$-2\zeta_{ll_{r2}}\omega_{ll_{r2}}$	-6.128 ^c	n/a	n/a

^aFixed in model structure.

^bEliminated during model structure determination.

^cFixed derivative tied to free derivative $Y_{\beta_{1s}} = -1 * X_{\beta_{1c}} - \omega_{ll_{r2}}^2 = 1.00 * -\omega_{ll_r}^2$, $-2\zeta_{ll_{r2}}\omega_{ll_{r2}} = 1.00 * -2\zeta_{ll_r}\omega_{ll_r}$.

Table 6. Identified G-matrix parameters for 120 knots model.

Derivative	Value	Cramer Rao (%)	Insensitivity (%)
X_{XP}	0 ^b	n/a	n/a
X_{XC}	0.3843	10.07	4.04
Y_{XP}	-5.023	22.14	3.161
Y_{XC}	0 ^b	n/a	n/a
Z_{XB}	7.028	3.611	1.629
Z_{XA}	0 ^b	n/a	n/a
Z_{XP}	0 ^b	n/a	n/a
Z_{XC}	-11.09	3.179	1.516
L_{XP}	-0.4864	9.439	3.872
L_{XC}	0 ^b	n/a	n/a
M_{XP}	0 ^b	n/a	n/a
M_{XC}	0.2648	3.308	1.195
N_{XB}	0 ^b	n/a	n/a
N_{XP}	0.8534	2.701	0.9511
Lf_{XB}	0.0359	4.882	0.6017
Lf_{XA}	-0.0205	5.131	1.117
Mf_{XB}	0.0461	4.083	0.6085
Mf_{XA}	0.009	6.692	1.79
τ_{XB}	0.0 ^b	n/a	n/a
τ_{XA}	0.0 ^b	n/a	n/a
τ_{XP}	0.0 ^b	n/a	n/a
τ_{XC}	0.1393	2.296	1.131

^aFixed in model structure.

^bEliminated during model structure determination.

Table 7. Cost functions for 120 knots model.

Transfer Function	Cost
\dot{u}/X_B	125.5
\dot{v}/X_B	76.13
\dot{w}/X_B	219.58
p/X_B	141.21
q/X_B	127.38
$q_{lead-lag}/X_B$	509.45
r/X_B	115
a_x/X_B	121.68
a_y/X_B	38.2
a_z/X_B	49.72
$(a_y)_2/X_B$	153.34
$(a_z)_2/X_B$	712.64
\dot{v}/X_A	76.13
\dot{w}/X_A	81.23
p/X_A	184.83
$p_{lead-lag}/X_A$	533.83
q/X_A	77.4
a_y/X_A	72.91
$(a_y)_2/X_A$	177.04
\dot{v}/X_P	99.28
\dot{w}/X_P	109.12
p/X_P	124.46
r/X_P	96.85
a_y/X_P	70.89
β/X_P	124.02
\dot{u}/X_C	150
\dot{w}/X_C	182
r/X_C	27.928
q/X_C	112
a_x/X_C	70.98
a_z/X_C	55.12
Average	135.57